IOPscience iopscience.iop.org

Home Search Collections Journals About Contact us My IOPscience

Plasma frequency and dielectric function dependence on doping and temperature for p-type indium phosphide epitaxial films

This article has been downloaded from IOPscience. Please scroll down to see the full text article.

2012 J. Phys.: Condens. Matter 24 435803

(http://iopscience.iop.org/0953-8984/24/43/435803)

View the table of contents for this issue, or go to the journal homepage for more

Download details:
IP Address: 131.96.4.103
The article was downloaded on 05/10/2012 at 15:51

Please note that terms and conditions apply.

J. Phys.: Condens. Matter **24** (2012) 435803 (8pp) doi:10.1088/0953-8984/24/43/435803

Plasma frequency and dielectric function dependence on doping and temperature for p-type indium phosphide epitaxial films

R C Jayasinghe[1], Y F Lao[1], A G U Perera[1], M Hammar[2], C F Cao[3] and H Z Wu[4]

[1] Department of Physics and Astronomy, Georgia State University, Atlanta, GA 30303, USA
[2] School of Information and Communication Technology (ICT), Royal Institute of Technology (KTH), Electrum 229, SE-164 40 Kista, Sweden
[3] State Key Laboratory of Functional Materials for Informatics, Shanghai Institute of Microsystem and Information Technology, Chinese Academy of Sciences, 865 Changning Road, Shanghai 200050, People's Republic of China
[4] Department of Physics, Zhejiang University, Hangzhou 310027, People's Republic of China

E-mail: uperera@gsu.edu

Received 21 July 2012, in final form 10 September 2012
Published 4 October 2012
Online at stacks.iop.org/JPhysCM/24/435803

Abstract
The optical properties of p-type InP epitaxial films with different doping concentrations are investigated by infrared absorption measurements accompanied by reflection and transmission spectra taken from 25 to 300 K. A complete dielectric function (DF) model, including intervalence band (IVB) transitions, free-carrier and lattice absorption, is used to determine the optical constants with improved accuracy in the spectral range from 2 to 35 μm. The IVB transitions by free holes among the split-off, light-hole, and heavy-hole bands are studied using the DF model under the parabolic-band approximation. A good understanding of IVB transitions and the absorption coefficient is useful for designing high operating temperature and high detectivity infrared detectors and other optoelectronic devices. In addition, refractive index values reported here are useful for optoelectronic device designing, such as implementing p-InP waveguides in semiconductor quantum cascade lasers. The temperature dependence of hole effective mass and plasma frequency is also reported.

(Some figures may appear in colour only in the online journal)

1. Introduction

Indium phosphide is a basic semiconductor material for infrared (IR) optoelectronic and photonic device fabrication devoted to future optical communication systems. The development of group-III phosphide based optoelectronic devices [1] depends on understanding the optical properties of phosphide materials and their alloys with doping and temperature. In a p-type InP semiconductor where free holes are present, intervalence band (IVB) transitions can occur among the split-off (so), light-hole (lh) and heavy-hole (hh) bands, each with two-fold spin degeneracy. Recent studies on p-type semiconductors have attracted attention for optical studies on the absorption properties using infrared dielectric function (DF) [2] as well as applications to heterojunction internal photoemission detectors [3]. Recently reported GaAs based internal photoemission type detectors [3, 4] have shown high operating temperature (up to 330 K) capability in the 1–3 and 8–14 μm IR wavelength ranges. Since the IVB and free-carrier (FC) absorption depend on the concentration of free holes, and the spin–orbit splitting energy of InP [5] is 108 meV, the total absorption coefficient of heavily doped

 © 2012 IOP Publishing Ltd Printed in the UK & the USA

InP can be higher than that of other materials such as p-GaAs. Therefore, a model dealing with the IVB transitions will be of interest for practical applications as well as for fundamental research. Furthermore, accurate simulation and design of device structures need proper handling of doping effects, including the IVB transitions for calculating optical constants. In this work, a DF model that takes into account IVB transitions was deduced with analytical expressions under the parabolic-band approximation. Although p-InP was used as a waveguide/current blocking layer in quantum cascade laser [6] (QCL) structures, information about its absorption properties would be useful for the overall modeling on the laser performance. In addition, p-InP can also be one of the important components in p–n laser diodes such as dual wavelength lasers based on the bipolar cascade laser [7] (BCL) structures and InGaAsP/InP laser diodes [8, 9]. Therefore, it is helpful to have knowledge of p-type InP thin film material properties such as absorption and refractive index for understanding/modeling these QCL structures and also focusing on the other kinds of laser structures which use optical properties of p-InP directly. Hence, the results reported in this manuscript would be useful in designing these device structures.

Infrared absorption in GaP [10] and InP [11] bulk crystals has been reported previously using two-phonon absorption spectroscopy, which also discuss the effect of higher-order terms of the primary phonons of those materials. A few studies have been reported based on density matrix theory [12] in the near-IR (1–3 μm) region for InP epitaxial films. However, detailed mid (3–14 μm) and far (14 μm and beyond) IR absorption (experimental or theoretical) studies for p-InP epitaxial films have not been reported, and also have not been modeled using the DF. Determination of crystalline quality and the free-carrier (FC) concentration can be characterized from the plasma frequency [13] and phonon mode dependency on polarized light [14] incident at oblique angles.

2. Experiment

The p-type InP epitaxial films were grown on semi-insulating InP substrates by gas source molecular beam epitaxy (GSMBE), for high (2.4×10^{19} cm^{-3}) doping, and metal organic vapor phase epitaxy (MOVPE), for low (1 and 3×10^{18} cm^{-3}) doping. The thickness of the substrate is 350 μm for GSMBE and 440 μm for MOVPE grown samples. The samples were back side polished in order to reduce the reflection losses and scattering from the surface. All measurements were performed with a Perkin–Elmer system 2000 Fourier transform infrared spectrometer (FTIR) along with a globar source, a HgCdTe detector with a KBr beamsplitter (for mid-IR), and a triglycine sulfate (TGS) detector with a 6 μm mylar beamsplitter (for far-IR). The spectral resolution was 4 cm^{-1}. For both the substrate sample and the film/substrate samples, transmittance was measured under normal incidence, while the reflectance was measured at near normal incidence with a gold mirror as a reference using the specular reflection accessory at room temperature. A helium closed cycle refrigerator system was used for the measurements from 25 to 275 K at 25 K intervals.

3. Theoretical models

3.1. Drude and Lorentz model for free-carrier absorption

The DF in the IR region is primarily determined by phonon and FC contributions [15]. The phonon contribution arises from collective lattice vibrational modes under the propagating electric field of the incident light. These phonon contributions are modeled using Lorentz oscillators. The FC plasma contribution, which is due to the interaction of FC with the electric field of the incident light, can be modeled using the classical Drude model [16] approximation. It has been successfully applied to p-GaAs [17] and n-GaN [18] using a single plasma frequency and damping constant along with the Lorentzian oscillator model. Hence, the DF can be presented in equation (1) for the IR region.

$$\varepsilon(\omega) = \varepsilon_\infty \left(1 - \frac{\omega_p^2}{\omega^2 + i\omega\gamma}\right) + \sum_j \frac{S_j \omega_{f,j}^2}{\omega_{f,j}^2 - \omega^2 + i\omega\Gamma_j} \quad (1)$$

where ω, ω_p, γ, and ε_∞ are the frequency of the incident light, FC plasma frequency, FC plasma damping and high frequency dielectric constant, respectively. Also, $\omega_{f,j}$, S_j, and Γ_j are the frequency of the jth Lorentzian oscillator (which represents the corresponding phonon frequency), oscillator strength, and oscillator broadening.

The intensity-transfer-matrix method [19] was used to calculate IR reflectance and transmittance spectra from the three-phase vacuum/film/substrate multilayer structure. The interface matrix $Q_{j-1,j}$ which represents the interaction of light between the $(j-1)$th and jth layers is given by

$$Q_{j-1,j} = \frac{1}{2\sqrt{\varepsilon_{j+1}}} \begin{pmatrix} (\sqrt{\varepsilon_j} + \sqrt{\varepsilon_{j-1}}) & (\sqrt{\varepsilon_j} - \sqrt{\varepsilon_{j-1}}) \\ (\sqrt{\varepsilon_j} - \sqrt{\varepsilon_{j-1}}) & (\sqrt{\varepsilon_j} + \sqrt{\varepsilon_{j-1}}) \end{pmatrix} \quad (2)$$

and the propagation matrix P_j for the light propagation in the jth layer with thickness d is described by

$$P_j = \begin{pmatrix} \exp(i2\pi\sqrt{\varepsilon_j}d/\lambda) & 0 \\ 0 & \exp(-i2\pi\sqrt{\varepsilon_j}d/\lambda) \end{pmatrix}. \quad (3)$$

The electric and magnetic fields in each layer can be obtained by repeating equations (2) and (3). The total transfer matrix M is the multiplication of the matrix in layer 0 through layer N ($j = 0$ representing the light incoming media), i.e., $M = \prod_{j=1}^{N} P_j Q_{j-1,j}$. The reflectance ($R$) and transmittance ($T$) are expressed by

$$R = \left|\frac{M_{21}}{M_{11}}\right|^2 \quad \text{and} \quad T = \frac{\mathrm{Re}(\sqrt{\varepsilon_N})}{\mathrm{Re}(\sqrt{\varepsilon_0})}\left|\frac{\det(M)}{M_{11}}\right|^2. \quad (4)$$

The multiple reflected beams from the substrate surfaces are added incoherently to neglect the phase information as described in [20]. Hence, the equation (4) is modified accordingly. The reflection and transmission spectra for the doped samples are shown in figure 1. The IR absorption was calculated from $A = 1 - T - R$ and shown in figure 2 for different doping levels. The transmission in

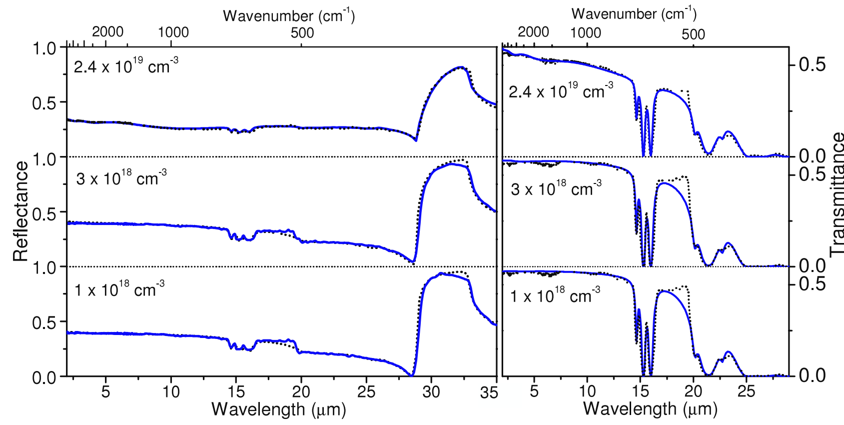

Figure 1. Experimental reflectance and transmittance spectra (dotted lines) of the sample having p-InP epilayers on InP substrate along with the best-fit results (solid lines) at 300 K. The transmission drastically reduces beyond 20 μm and is almost zero in the 30–35 μm range. Therefore this region for transmission is not shown. The top axis represents a wavenumber (cm^{-1}) scale which is equal to 10 000/λ (μm).

30–35 μm range is near zero; hence not shown in the figure. There is a step around 20 μm, as can be seen in reflection, transmission and absorption spectra (see figures 1 and 2), which is similar to reports for GaAs [21] due to multi-phonon absorption. This feature is a consequence of the substrate's transparency below 20 μm, which allows a contribution to the observed reflectivity from light returning from the substrate's back surface, which is in agreement with the theoretical model (especially for highly doped samples). However, the mismatch between calculated and experimental data around this feature will not affect the other results. The small difference is due to the Lorentzian shape of the oscillators. Due to phonon absorption and the Reststrahlen effect, transmission decreases drastically above 20 μm.

Even though there are many higher-order phonon frequencies [10] associated with InP material, only eight Lorentz oscillators (as shown by arrows in figure 2) were implemented to study the phonon absorption, depending on their strength in absorption. The oscillator parameters for the substrate are given in table 1. The first oscillator is the primary transverse optical (TO) phonon in InP and other oscillators are assigned to different combinations of TO and longitudinal optical (LO) phonons at different critical points in the Brillouin zone, as given in [11]. The best-fit parameter values in equation (1) are found using a Levenberg–Marquardt algorithm [22]. The reflectance and transmittance spectra were used to derive $\varepsilon(\omega)$ using the fitting procedure. The value of ε_∞(9.6) was taken as a fixed parameter [12]. The ω_p for FC with effective mass (m^*) and carrier concentration (n_p) can be found by

$$\omega_p = \sqrt{\frac{n_p e^2}{\varepsilon_0 \varepsilon_\infty m^*}} \Big/ 2\pi c. \quad (5)$$

SI units should be used with this equation. The m^* is taken as an average of hh and lh masses [23], $(m_{lh}^{3/2} + m_{hh}^{3/2})/(m_{lh}^{1/2} + m_{hh}^{1/2})$, where ($m_{hh}^* = 0.58$, $m_{lh}^* = 0.12$, $m_{so}^* = 0.12$) [24]. n_p was obtained from Hall measurements and is used as the initial value in the fitting program and the final ω_p values extracted from the fittings are listed in table 2.

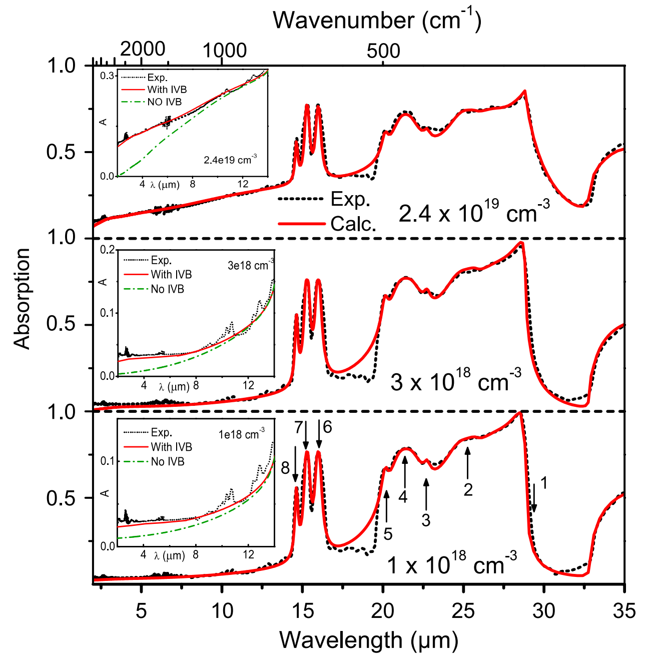

Figure 2. Experimental absorption spectra (dotted lines) of the p-InP films on InP substrate along with their best-fit results (solid lines) at 300 K. For clarity, each spectrum is successively shifted by 1 in the vertical direction. The arrows indicate the location of each Lorentzian oscillator. The insets show the enlarged region (2–14 μm) where IVB absorption is expected and show the absorption with and without IVB transitions. The IVB absorption increases with doping and overshadows the weaker higher-order phonon peaks in the 10–13 μm range.

The oscillator/phonon frequencies of the semi-insulating InP substrate were initially determined by cross-referencing the values reported [11] for bulk InP. Once those frequencies were fixed, the oscillator strength and broadening parameters were optimized for the first oscillator, since it is the strongest [11]. These parameters determine the shape of the

Table 1. Fitting parameters for each Lorentz oscillator of semi-insulating InP substrate at 300 K. Here ω_f, S, and Γ are phonon frequency, oscillator strength, and broadening constant, respectively, as given in equation (1). Best-fit 90% confidence limits are given in parentheses.

	Oscillator number							
	1	2	3	4	5	6	7	8
ω_f (cm^{-1})	305.5 (0.5)	386.0 (0.5)	440.0 (0.5)	467.1 (0.5)	496.5 (0.5)	625.5 (0.5)	654.0 (0.5)	683.3 (0.5)
S	2.78 (0.01)	0.022 (0.001)	0.0002 (0.0001)	0.004 (0.001)	0.0003 (0.0001)	0.001 (0.001)	0.001 (0.001)	0.0002 (0.0001)
Γ (cm^{-1})	1.1 (0.5)	12 (1)	8 (1)	25 (2)	10 (1)	6.5 (1)	6 (1)	8 (1)
Reference [11]	TO(Γ)	TO(X) + TA(X)	$W_3 + W_4$	$W_1 + W_4$	LO(L) + LA(L)	2TO(L)	LO(Γ) + TO(Γ)	2LO(L)

Table 2. Fitting parameters for computing the contributions of FC, phonon absorption, and IVB transitions to the DF (at 300 K). Here, d, ω_p, and γ are thickness of the epi-layer, FC plasma frequency, and FC plasma damping, respectively. S_1 and Γ_1 are strength and broadening of the first oscillator. A and Γ are strength and broadening for each IVB transition. First column shows the nominal doping values from Hall measurements. Best-fit 90% confidence limits are given in parentheses.

Sample (cm^{-3})	d (nm)	ω_p (cm^{-1})	γ (cm^{-1})	S_1	Γ_1 (cm^{-1})	$A_{\text{lh-hh}}$ (meV^2 cm^3)	$A_{\text{so-hh}}$ (meV^2 cm^3)	$\Gamma_{\text{lh-hh}}$ (meV)	$\Gamma_{\text{so-hh}}$ (meV)
2.4×10^{19}	1190 (2)	649 (3)	1318 (9)	3.10 (0.01)	1.7 (0.5)	2.1 (0.2)	1.2 (0.1)	102 (5)	110(2)
3×10^{18}	675 (2)	252 (3)	512 (8)	2.82 (0.01)	1.2 (0.5)	1.9 (0.2)	1.1 (0.1)	53 (5)	72 (2)
1×10^{18}	675 (2)	144 (3)	304 (8)	2.80 (0.01)	1.1 (0.5)	1.9 (0.2)	1.1 (0.1)	22 (5)	13 (2)

reflectance spectra mainly in the far-IR region (26–35 μm) and increase with doping (as listed in table 2). The parameters for the other oscillators were optimized using both reflectance (R) and transmittance (T) spectra, as shown in figure 1. The IR absorption spectra are shown in figure 2. The variation of strength and broadening values for other oscillators due to doping is within the fitting errors.

3.2. Intervalence band transitions

The intervalence band (IVB) transitions yield an additive contribution to the dielectric function. For p-type semiconductors, three IVB transitions can occur among the valence bands (split-off (so), light-hole (lh), and heavy-hole (hh) bands). Under an approximation of using parabolic-band structures, which is valid for most of the doping concentrations since transitions primarily occur around the Γ point. The modeling details have been described in [2]. The following analytic expressions are given only for the imaginary component and the real component is obtained by the Kramers–Kronig transformations.

The IVB contribution to the dielectric function can be expressed by [2],

$$\varepsilon_2^{\text{IVB}}(E) = \varepsilon_2^{\text{lh-so}}(E) + \varepsilon_2^{\text{hh-so}}(E) + \varepsilon_2^{\text{lh-hh}}(E). \qquad (6)$$

For a transition taking place between bands a and $b(a, b = \text{so, lh, hh})$, the DF is given by

$$\varepsilon_2^{ab}(E) = \frac{A_{ab}p\,|E - (E_{b0} - E_{a0})|^{\frac{3}{2}}}{E^2\,(k_B T)^{\frac{3}{2}}} \left(e^{\frac{E_a}{k_B T}} - e^{\frac{E_b}{k_B T}}\right) C_{\text{FD}}^{ab} \qquad (7)$$

where p is the hole concentration, k_B is the Boltzmann constant, T is the temperature, and $E_{a(b)}$ is given by the parabolic-band form, $E_{a(b)} = -E_{a(b)0} - \hbar k^2/2m^*_{a(b)}$ with $E_{a(b)}$ and $m^*_{a(b)}$ being the band-edge energy and effective mass for band $a(b)$. In equation (7), E_a and E_b are determined by $E_a - E_b = E$, and A_{ab} accounts for the transition strength and other effects such as the non-parabolicity of energy bands off the Γ point. The fittings [2] to p-GaAs show that A_{ab} is constant except at the higher doping range above 10^{19} cm^{-3} as a result of the band non-parabolicity. Here, A_{ab} is expressed as

$$A_{ab} = \frac{16 C_0 B_{ab}}{\hbar^2 (m_a^{*3/2} + m_b^{*3/2})} \left(\frac{\pi m_a^* m_b^*}{m_a^* - m_b^*}\right)^{\frac{5}{2}}. \qquad (8)$$

Here, C_{FD}^{ab} is a constant related to the Fermi level.

$$C_{\text{FD}}^{ab} = \frac{\exp\{-[E_f + k_B T \ln(\frac{P}{N_v})]/k_B T\}}{\{1 + \exp[(E_a - E_f)/k_B T]\}\{1 + \exp[(E_b - E_f)/k_B T]\}} \qquad (9)$$

with E_f the energy of the hole quasi-Fermi level and N_v the sum of hh and lh effective density of states. For low doping concentrations, E_f lies above the VB top, yielding $C_{\text{FD}}^{ab} \approx 1$. The non-parabolicity as in the actual VBs off the Γ point causes varied m^* and A_{ab}. At wavevectors where hole transitions will see the parallel bands, A_{ab} can be significantly increased.

4. Results and discussions

To obtain the IVB DF, parameters representing the strength (A_{ab}) and line-shape broadening (Γ_{ab}) of transitions were determined by fitting experimental data with the model output. Compared to p-GaAs [2], the case of p-InP is complicated by the small spin–orbit splitting ($\Delta_{\text{so}} = 108$ meV). Therefore, so–hh and lh–hh absorption regions are merged, unlike in

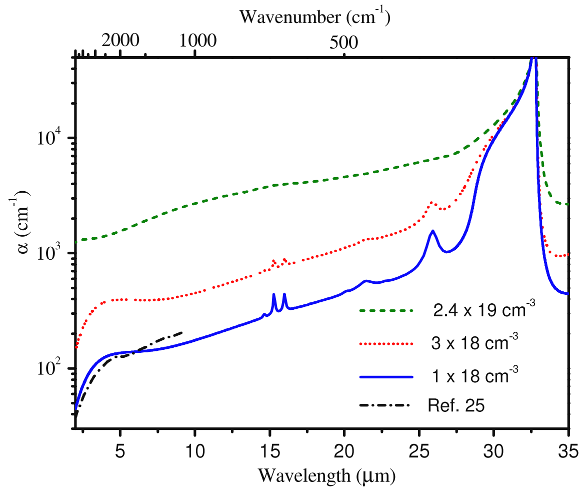

Figure 3. Calculated absorption coefficient at 300 K. The strong absorption peak around 32.7 μm (306 cm^{-1}) is due to Reststrahlen absorption of the lattice structure. The weak peaks are due to the difference in phonon absorption between the doped layer and the substrate. The theoretical values are compared with the data taken from [25] for 1×10^{18} cm^{-3}.

p-GaAs. Because of this small Δ_{so}, much of the absorption due to direct IVB transitions occurs in a region of the IR where lattice absorption and FC absorption are strong. Based on the DF model in [2], a fit to the absorption spectra is shown in figure 2. The fitting parameters are given in table 2. The insets in figure 2 show the absorption with and without IVB transitions in the 2–14 μm region. This shows that the difference comes from the IVB transitions. It can also be seen that IVB absorption increases with doping. The small absorption peaks visible (10–13 μm range) are due to higher-order phonon frequencies [10] and are prominent in low-doping samples. In view of these results, the so–hh and lh–hh transitions have a larger broadening constant for higher doping levels. This is reasonable since the energy of transitions occurring around the Fermi surface shifts toward the higher values. The resultant effect is a large quantity of holes being populated into the higher energy states. The so–lh transition is relatively weak due to the low occupation of the holes in the lh band [2]. The strength of the IVB transitions is controlled by the concentration of the free holes and is in competition with intra-band FC absorption. The total absorption coefficient extracted from the DF is plotted in figure 3 with comparisons to the experimental [25] data for 1×10^{18} cm^{-3}. The reason for higher values in absorption coefficient in the MIR region, even though it is not prominent in the absorption spectra, is that the substrate is optically much thicker compared to the doped thin film layer.

The temperature dependence of ω_p, γ, and phonon frequencies has been studied from 25 to 300 K, as shown in figure 4. The empirical formula deduced is $\omega_p = \omega_0 + a_1 e^{-1000/Tb1}$, where $a_1 = 107, b_1 = 1.75 + 0.008(n_p/10^{18})$, and $\omega_0 = 20.8 + 137.2(n_p/10^{18})$. Here, n_p, ω_p, and T are in cm^{-3}, cm^{-1}, and K, respectively. According to this equation the plasma frequency decreases exponentially with decreasing temperature. The parameters are given in terms of hole concentration (n_p) at 300 K. Free-carrier intra-band (same energy band) absorption is an indirect process and is mediated by phonons [26] which supply the additional momentum required for the overall energy and momentum conservation and are responsible for the temperature dependence of optical features. Also, ω_p depends on hole density and hole effective mass. Since the damping and plasma frequency are inter-connected, the fitting parameters for damping are given in terms of the fitting parameters of plasma frequency. Therefore, an empirical formula deduced for plasma damping is $\gamma = \gamma_0 + a_2 e^{-1000/Tb2}$, where, $a_2 = 1.72a_1 + 5.26(n_p/10^{18})$, $b_2 = 4.76 + 1.15b_1$, and $\gamma_0 = 11.49 + 2.28\omega_0$. This indicates that at low temperature, the mobility of free carriers increases. The saturation level at low temperatures is given by ω_0 and γ_0. In addition, the phonon frequencies increase with decreasing temperature ($\omega_f = 633 - 0.02$ T). Even though Raman measurements [27] of the temperature dependence of phonons indicate that this dependence is not linear for oscillator #1, the linear approximation for phonon frequency shift is good enough to describe the results in the mid-infrared region for oscillators #6, #7, and #8. The temperature dependence of these phonons is shown in the inset of figure 4(b). The low temperature measurements were not carried out at in the far infrared region ($\lambda > 22$ μm) where oscillator #1 is located.

The effective mass of holes is an important parameter that affects the mobility, electrical resistivity, and free-carrier optical response of a semiconductor. Most commonly, the effective mass is simply designated by their values at their respective band edges. However, for high carrier concentrations or under cryogenic temperatures, the effective masses can vary significantly from their band-edge values. These variations are due to the characteristics of the semiconductor band structure, such as non-parabolicity and the splitting of the bands at valence band edges. Although there have been a few theoretical attempts to understand the temperature dependence of the effective mass [28], experimental studies in cryogenic temperatures are not yet reported for p-InP. The calculated density of states hole effective mass reported in [28] shows a 50% increase from room temperature to 80 K for 1×10^{18} cm^{-3}. Due to the large density of states, heavy holes play a dominant role in optical transitions. The valence bands in III–V compounds are warped from spherical symmetry and it has been shown that, depending on the method of measurement, heavy-hole mass values ranging from 0.3 to $0.8m_0$ are obtained from theoretical studies for InP [29]. A good review of theoretical and experimental evaluations of the InP hole effective mass at room temperature is reported in [29]. In our work, the plasma frequency variation at different frequencies has been used to extract the effective mass dependency with temperature, assuming that the plasma frequency change is mainly due to a change in the effective mass. This is shown in figure 5 for the highest doped sample (dots). The increase in effective mass is 5% as the temperature is lowered from 300 to ~100 K. The effective mass stays constant for temperatures below 100 K. Since there is no experimental data reported at low temperature to the best of our knowledge, to compare our results two theoretical methods have been applied as described below.

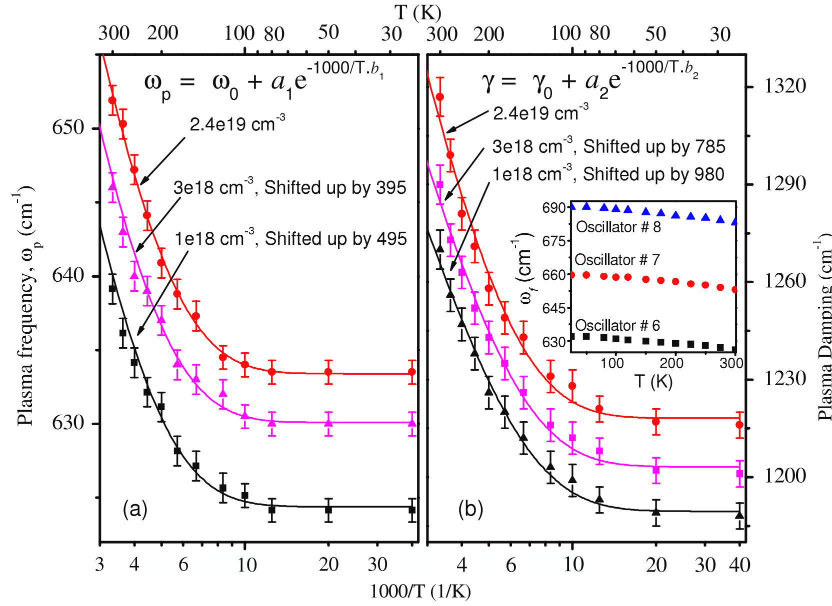

Figure 4. The temperature dependence of (a) plasma frequency ω_p and (b) plasma damping γ is shown. Solid lines are the best fits to the experimental data. Data for two lowest doped samples are shifted up for comparison. The parameters used in empirical formulas (shown in the figures) depend on the 300 K carrier concentration. ω_0 and γ_0 indicate the saturation level at low temperatures. The inset in (b) shows the variation of phonon frequency with temperature.

The hole effective mass (m_h^*) variation with temperature for group III–V semiconductors can be found by using the following expression as reported by Adachi [30]. The temperature dependence of m_h^* assumes that the hole mass varies with temperature shift of the bandgap (E_g).

$$m_h^*(T) = m_h^*(0)\frac{E_g(T)}{E_g(0)}. \qquad (10)$$

Here $m_h^*(0)$ and $E_g(0)$ are the mass and E_g values at $T = 0$ K, respectively. The bandgap variation with temperature is taken as $E_g(T) = E_g(0) - \alpha T^2/(\beta + T)$. Bandgap narrowing [31] due to high doping is also considered. There are discrepancies among bandgap parameters and several values have been tried out, as listed in table 4. The different values could be due to different growth conditions. Since, the shape of the curve depends on the temperature variation of the bandgap of the material, the parameters in $E_g(T)$ equation can be varied to obtain a better fit to the experimental data. In fact, the values reported by Pavesi *et al* [32] give the best fit to our data. The calculated m_h^* using these data is plotted in figure 5. It can be seen that Adachi's method gives comparable results to the experimental data. Adachi's method is also tested for the electron effective mass for n-InP data [33], which shows a similar trend. The same trend (effective mass decreasing with increasing temperature) is observed for electrons in n-InP, as reported by Schneider *et al* [33], and for holes in p-InP, as reported by Hansen *et al* [28].

For semiconductor device designs, an accurate model for the refractive index is crucial, e.g., for determining the optical field distribution in a structure, especially in infrared photodetector or QC laser structures. By using the DF model, the spectra of refractive index can be easily calculated. With increase in doping, the refractive index is

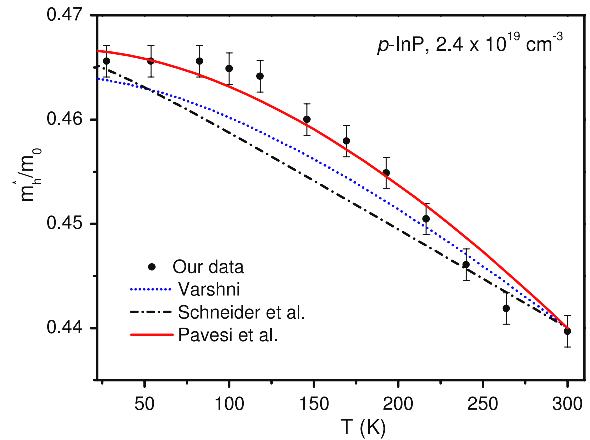

Figure 5. The temperature dependence of hole effective mass (m_h^*) is shown. Our m_h^* data (dots with error bars) are extracted from the plasma frequency (ω_p) using equation (5), where ω_p was obtained from the best fitting spectra to the experimentally measured absorption data for the highest doped sample (2.4×10^{19} cm^{-3}). The calculated values for m_h^* using equation (10) are also shown for different bandgap variation cases: [33, 39, 32].

reduced, with a strong reduction at low photon energies. The calculated refractive index using DF is shown in figure 6(a) for 1.2–24 μm. The refractive index difference (Δn) between doped and undoped samples is shown in figure 6(c). Undoped InP data is compared with values obtained from the three-term Sellmeier equation [34], as shown in figure 6(b). This Sellmeier equation can be used to predict refractive index $n(\lambda)$ in the 1.2–13 μm wavelength range as given below,

$$n^2(\lambda) = A + \frac{B_1\lambda^2}{\lambda^2 - C_1^2} + \frac{B_2\lambda^2}{\lambda^2 - C_2^2} \qquad (11)$$

Table 3. Samples used and Sellmeier coefficients (as given in equation (11)) as determined from least-squares fit to refractive index curves. First column shows the nominal doping values from Hall measurements at room temperature. A, B_1, and C_1 are corresponding to the range 1.2–2.5 μm and B_2, C_2 corresponding to 2.5–12 μm range (2.5–8 μm range for 2.4×10^{19} cm^{-3}). The tolerance is given in parentheses.

Sample (cm^{-3})	A	B_1	C_1	B_2	C_2
Undoped[a]	7.255	2.316	0.6263	2.765	32.935
Substrate	7.21 (0.01)	2.342 (0.008)	0.6263 (0.0002)	2.83 (0.01)	32.45 (0.01)
1×10^{18}	7.05 (0.01)	2.472 (0.008)	0.6268 (0.0005)	4.11 (0.01)	32.01 (0.03)
1.9×10^{18}[b]	6.95 (0.01)	2.53 (0.01)	0.6280 (0.0005)	—	—
3×10^{18}	6.91 (0.01)	2.56 (0.01)	0.6310 (0.0005)	5.26 (0.01)	31.90 (0.03)
5.3×10^{18}[b]	6.71 (0.01)	2.61 (0.02)	0.6361 (0.0005)	—	—
6.2×10^{18}[c]	6.62	2.66	0.6403	—	—
2.4×10^{19}	6.56 (0.03)	2.71 (0.05)	0.6453 (0.0005)	10.34 (0.08)	30.19 (0.09)

[a] Sellmeier coefficients taken from [34].
[b] Absorption coefficients taken from [12] to calculate A, B_1 and C_1.
[c] Sellmeier coefficients taken from [37].

Table 4. Values of the parameters for the energy bandgap dependence of InP with temperature. Here, $E_g(T) = E_g(0) - \alpha T^2/(\beta + T)$.

$E_g(0)$ (eV)	α ($\times 10^{-3}$) (meV K^{-1})	β (K)	Validity range (K)
1.424 ± 0.005[a]	1.02 ± 3	823 ± 200	0–250
1.432 ± 0.007[b]	0.41 ± 0.03	136 ± 60	77–870
1.4206[c]	0.49	327	0–300
1.4236[d]	0.29	30.63	0–300

[a] Reference [32].
[b] Reference [38].
[c] Reference [39].
[d] Reference [33].

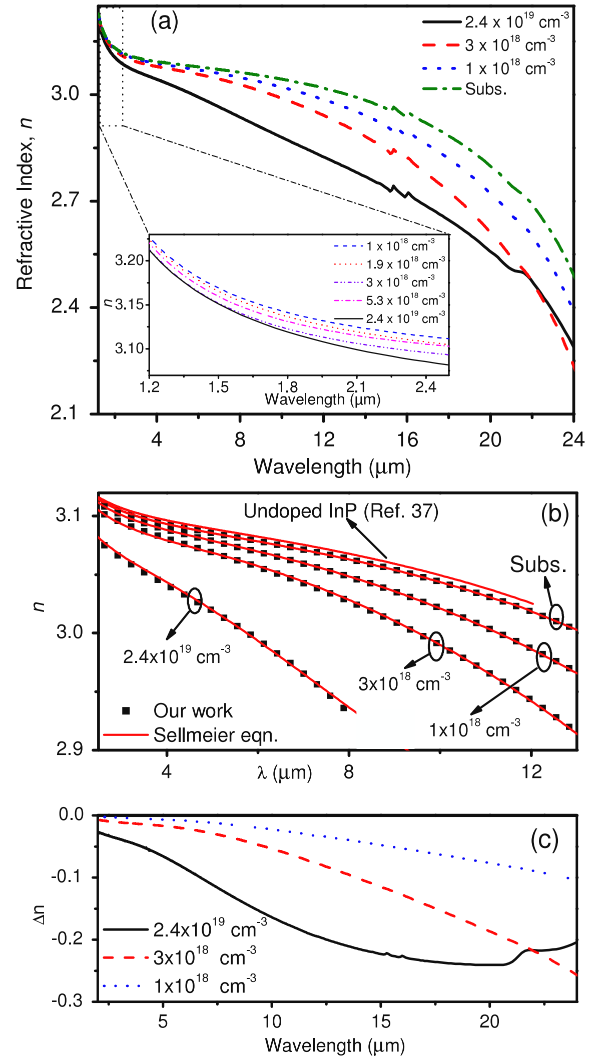

Figure 6. Calculated refractive index is shown in (a) for different doping concentrations. Inset in (a) shows the zoomed-in region for 1.2–2.5 μm for clarity. The least-square fittings made using equation (11) are shown in (b). In (c), the difference in refractive index (Δn) between the undoped and doped InP is shown. A strong reduction in n in the low-energy region and higher doping samples is the result of increased absorption due to the FC and IVB processes. The highest doped sample shows an increase in n at long wavelengths (>22 μm).

where the first and second terms correspond to short-wavelength absorption (fundamental bandgap absorption) contributions to the refractive index at the near-infrared region, and the third term denotes the contribution from the far infrared Reststrahlen effect at the mid-infrared region. B_1 and B_2 are the strengths and C_1 and C_2 reflect the approximate positions of the Lorentzian oscillators, which represent the absorption mechanisms stated above. The Sellmeier coefficients (see table 3) were determined by obtaining least-square fits to the refractive index extracted from DF, as shown in figure 6(b) for comparison. In order to determine A, B_1 and C_1, only the 1.2–2.5 μm region is considered, assuming that there is no effect from the third term in this region, since after 2.5 μm the shape of the spectra changes only due to the Reststrahlen features at far-IR (28–35 μm). A similar assumption is used for undoped and n-doped InP, as reported in [35]. Likewise, B_2 and C_2 were determined using 2.5–13 μm data while keeping previously calculated A, B_1 and C_1 values fixed. The DF is obtained for additional dopings by fittings to the experimental absorption coefficients reported in [12]. The increase in C_1 with doping is due to bandgap narrowing and the decrease in C_2 is due to blue-shifting of the plasma frequency due to free-carrier absorption. These results will be useful for InP based optoelectronic device design and characterization, especially for mid-IR photodetectors and quantum cascade lasers. Even though the refractive index decreases with doping, beyond 22 μm the magnitude of Δn for highest doping starts to decrease. With increasing doping, the refractive index is reduced because of strong free-carrier intra-band absorption as a result of the red-shift of the plasma

frequency. The phonon absorption features (around 16 and 21.5 μm) are more prominent in the highest doped sample, as seen in figure 6(c). For semiconductor devices, the operating wavelength could be selected in the low-absorption region, where the index of refraction is similar to the undoped materials. However, several crucial spectral regions, e.g., the 8–14 μm atmospheric window, fall in the IVB range where refractive index is sensitive to the doping concentrations. Therefore, a proper consideration of the IVB contributions is necessary to determine an accurate refractive index and is simultaneously useful in the optimum design of related optoelectronic devices. Also, several modern applications, such as wavelength division multiplexing, the design of Bragg reflectors or modal calculations, require an accurate knowledge of InP refractive index in the 1.3–1.5 μm range.

5. Summary

In summary, mid and far-IR absorption have been investigated in three different p-type InP samples along with the InP substrate. The absorption coefficient and refractive index extracted from the DF will be useful for various applications, including IR split-off band detectors designs [36]. One of the atmospheric windows, 8–14 μm is a crucial spectral region that falls into the scope of IVB effects in which the refractive index is sensitive to the doping concentration. Therefore, the corresponding optical constants along with doping dependence of refractive index will be useful for modeling semiconductor structures. The temperature dependence of ω_p and hole effective mass will also be useful for designing mid- and far-IR group-III phosphide based detectors and QC lasers operating at or below room temperature.

Acknowledgments

This material is based upon work supported by, or in part by, the US Army Research Laboratory and the US Army Research Office under contract/grant numbers W911NF-08-1-0448/W911NF-12-2-0035 and the US NSF under grant number ECCS-1232184. The authors acknowledge Greggory Rothmeier for help in manuscript preparation.

References

[1] Sengupta D K *et al* 1996 *Appl. Phys. Lett.* **69** 3209
[2] Lao Y F and Perera A G U 2011 *J. Appl. Phys.* **109** 103528
[3] Jayaweera P V V, Matsik S G, Perera A G U, Liu H C, Buchanan M and Wasilewski Z R 2008 *Appl. Phys. Lett.* **93** 021105
[4] Lao Y F, Pitigala P K D D P, Perera A G U, Liu H C, Buchanan M, Wasilewski Z R, Choi K K and Wijewarnasuriya P 2010 *Appl. Phys. Lett.* **97** 091104
[5] Vurgaftman I, Meyer J R and Ram-Mohan L R 2001 *J. Appl. Phys.* **89** 5815
[6] Bour D P and Corzine S W 2006 *US Patent Specification* US 2006/0203865 Al
[7] Yan J, Cai J, Ru G, Yu X, Choa F-S and Fan J 2005 *Conf. on Lasers and Electro-Optics CMFF5* p 571
[8] Kajanto M, Chen T R, Zhuang Y H and Yariv A 1990 *IEEE J. Quantum Electron.* **26** 1895
[9] Bourillot E, David T, Lacroute Y and Lesniewska E 2008 *J. Opt. Soc. Am.* B **25** 1888
[10] Koteles E S and Datars W R 1976 *Solid State Commun.* **19** 221
[11] Ulrici B and Jahne E 1976 *Phys. Status Solidi* b **74** 601
[12] Kakimoto S and Watanabe H 1999 *J. Appl. Phys.* **85** 1822
[13] Hu Z G, Strassburg M, Dietz N, Perera A G U, Asghar A and Ferguson I T 2005 *Phys. Rev.* B **72** 245326
[14] Hu Z G, Weerasekara A B, Dietz N, Perera A G U, Strassburg M, Kane M H, Asghar A and Ferguson I T 2007 *Phys. Rev.* B **75** 205320
[15] Adachi S 1994 *GaAs and Related Materials* (Singapore: World Scientific)
[16] Blakemore J S 1982 *J. Appl. Phys.* **53** R123
[17] Rinzan M B M, Esaev D G, Perera A G U, Matsik S G, Von Winckel G, Stintz A and Krishna S 2004 *Appl. Phys. Lett.* **85** 5236
[18] Talwar D N 2010 *Appl. Phys. Lett.* **97** 051902
[19] Noh T W, Song P H, Lee S-I, Harris D C, Gaines J R and Garland J C 1992 *Phys. Rev.* B **46** 4212
[20] Djurisic A, Chan Y and Li E H 2002 *Mater. Sci. Eng.* R **38** 237
[21] Songprakob W, Zallen R, Liu W K and Bacher K L 2000 *Phys. Rev.* B **62** 4501
[22] Press W H, Flannery B P, Teukolsky S A and Vetterling W T 1986 *Numerical Recipes* (Cambridge: Cambridge University Press)
[23] Songprakob W, Zallen R, Tsu D V and Liu W K 2002 *J. Appl. Phys.* **91** 171
[24] Yu P Y and Cardona M 2005 *Fundamentals of Semiconductors: Physics and Materials Properties* (Berlin: Springer)
[25] Henry C H, Logan R A, Merritt F R and Luongo J P 1983 *IEEE J. Quantum Electron.* **19** 947
[26] Kioupakis E, Rinke P, Schleife A, Bechstedt F and Walle C G V D 2010 *Phys. Rev.* B **81** 241201(R)
[27] Irmer G, Wenzel M and Monecke J 1996 *Phys. Status Solidi* b **195** 85
[28] Hansen K, Peiner E, Schlachetzki A and Ortenberg M V 1994 *J. Electron. Mater.* **23** 935
[29] Osinski M 1990 *2nd Int. Conf. on Indium Phosphide and Related Materials (Denver, CO)* p 330
[30] Adachi S 2005 *Properties of Group-IV, III–V and II–VI Semiconductors* (Chichester: Wiley)
[31] Jain S C, McGregor J M and Roulston D J 1990 *J. Appl. Phys.* **68** 3747
[32] Pavesi L, Piazza F, Rudra A, Carlin J F and Ilegems M 1991 *Phys. Rev.* B **44** 9052
[33] Schneider D, Rurup D, Schonfelder B and Schlachetzki A 1996 *Z. Phys.* B **100** 33
[34] Bass M 1995 *Handbook of Optics* 2nd edn, vol 2 (New York: McGraw Hill)
[35] Martin P, Skouri E M, Chusseau L, Alibert C and Bissessur H 1995 *Appl. Phys. Lett.* **67** 881
[36] Matsik S G, Jayaweera P V V, Perera A G U, Choi K K and Wijewarnasuriya P 2009 *J. Appl. Phys.* **106** 064503
[37] Whalen M S 1982 *J. Appl. Phys.* **53** 4340
[38] Hang Z, Shen H and Pollak F H 1990 *Solid State Commun.* **73** 15
[39] Varshni Y P 1967 *Physica* **34** 149